RESEARCH ARTICLE

Key Points:
- We conduct dynamic rupture simulations to determine the frictional parameters on the fault, with constraints from near-field observations
- The average slip-weakening distance of 2015 M_w7.8 Nepal earthquake is ~0.6 m and the average fracture energy is ~1.4 × 10^6 J/m^2
- Such approach can be used to determine the frictional parameters on seismogenic faults in general, which serve for seismic hazard assessment

Supporting Information:
- Supporting Information S1
- Movie S1

Correspondence to:
H. Yang,
hyang@cuhk.edu.hk

Constraining Frictional Properties on Fault by Dynamic Rupture Simulations and Near-Field Observations

Huihui Weng[1] (iD) and Hongfeng Yang[1,2] (iD)

[1]Earth System Science Programme, Faculty of Science, The Chinese University of Hong Kong, Hong Kong, China, [2]Shenzhen Research Institute, The Chinese University of Hong Kong, Shenzhen, China

Abstract Frictional properties of seismogenic faults play critical roles in earthquake generation and rupture propagation. Although laboratory measurements have well revealed the frictional parameters of a variety of rock samples, those on seismogenic faults remain difficult to determine due to the strong trade-off between critical slip-weakening distance (d_0) and strength drop. Here we conduct dynamic rupture simulations to determine the frictional parameters on the fault where the 2015 M_w7.8 Nepal earthquake occurred, with constraints from near-field seismic and geodetic observations, and kinematic source models. By utilizing different trade-off patterns of source parameters and multiple observations for the first time, we can determine the frictional parameters of the seismogenic fault. The best fit dynamic model yields a d_0 value of ~0.6 m, in contrast to the previous kinematical estimation of ~5 m (Galetzka et al., 2015, https://doi.org/10.1126/science.aac6383). The average fracture energy of this event is $\overline{G_C} \simeq 1.4 \times 10^6$ J/m^2. Such approach can be used to determine the frictional parameters on seismogenic faults, which could serve for seismic hazard assessment by predicting ground motion from dynamic rupture simulations.

1. Introduction

Frictional properties of rocks hold key information of earthquake physics, yet are mostly measured in laboratory experiments (e.g., Di Toro et al., 2011). The frictional behavior of rocks in laboratory experiments could be approximated as a linear slip-weakening relation (Ida, 1972), in which the frictional resistance decreases from the static to dynamic level over the critical slip-weakening distance (d_0), an important parameter governing earthquake rupture dynamics. Many seismic studies have attempted to constrain d_0 in the field for several earthquakes based on dynamic (Dalguer et al., 2003; Dunham & Archuleta, 2004; Goto & Sawada, 2010; Ma et al., 2008; Nielsen & Olsen, 2000; Olsen et al., 1997; Peyrat & Olsen, 2004) and kinematic rupture models (Galetzka et al., 2015; Ide & Takeo, 1997; Tinti et al., 2004), as well as direct estimations from near-field ground motion observations (Fukuyama & Mikumo, 2007; Kaneko et al., 2017; Mikumo & Yagi, 2003). However, large uncertainties of the values of d_0 from seismological methods still remain (Ide & Takeo, 1997; Olsen et al., 1997), mostly because of the intrinsic trade-off between d_0 and strength drop (the difference of static and dynamic frictional resistance) (Goto & Sawada, 2010; Guatteri & Spudich, 2000). Here we determine the d_0 on the seismogenic fault of the 25 April 2015 M_w7.8 Nepal earthquake from spontaneous dynamic rupture simulations, constrained by near-field seismic, geodetic observations, and kinematic source models, which can significantly remove the trade-offs.

On 25 April 2015, an M_w7.8 earthquake has struck central Nepal, 80 km northwest of Kathmandu, and produced strong shaking that caused extensive damage and killed more than 8500 people (Sapkota et al., 2016). The rupture starts at a hypocentral depth of ~15 km and propagates eastwards along the lower edge of the locked portion of the Main Himalayan Thrust (Avouac et al., 2015), where the Indian and the Eurasian plates collide at a rate of ~18 mm/yr (Lavé & Avouac, 2000). Moment tensor solutions show that this earthquake was a nearly pure double-couple reverse faulting event, with the fault plane estimated to have a strike of 293°, a dip angle of 7–10°, and a rake of 95–100° (Avouac et al., 2015; Galetzka et al., 2015; Wei et al., 2018). The final slip distribution and rupture speed obtained from kinematic inversions and backprojection methods consistently show that this earthquake had a relative simple rupture pattern with an average speed of 2.8–3.2 km/s (Fan & Shearer, 2015; Grandin et al., 2015; Lay et al., 2016; Liu et al., 2016; Wei et al., 2018; Yagi & Okuwaki, 2015; Yin et al., 2017; Yue et al., 2016) (Figure 1a and Table 1). A number of seismic and geodetic apparatus, which have been installed in this region over past 20 years, provide a unique opportunity to investigate the rupture process of this event and the frictional properties of the seismogenic fault.
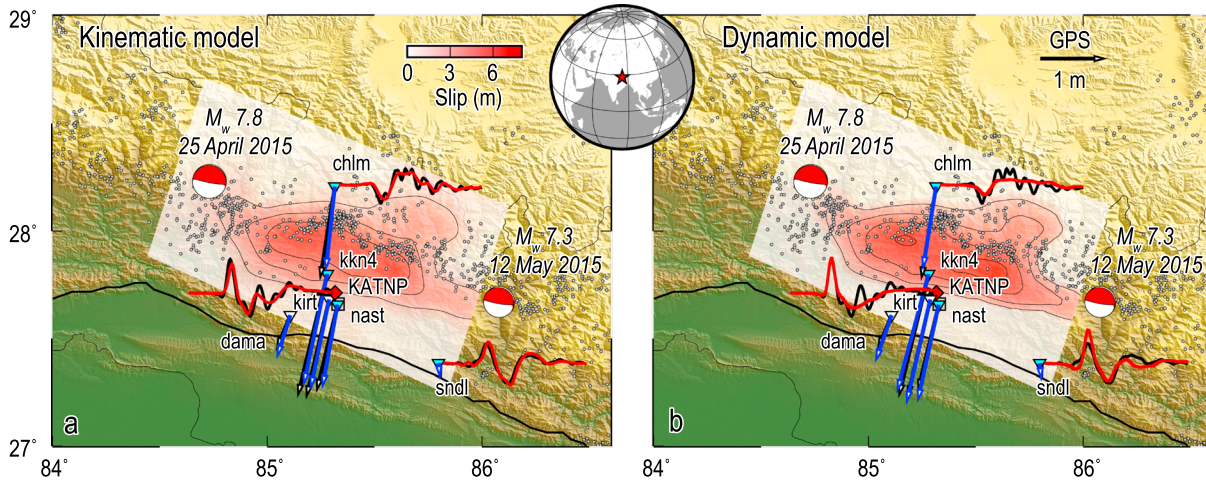
Figure 1. Kinematic and dynamic models of the 2015 Nepal Gorkha M_w7.8 earthquake. (a) The kinematic coseismic slip (red colors) with contours per 0.5 m is adapted from Wei et al. (2018). Cyan inverted triangles are the high-rate (5 Hz) GPS stations, and white inverted triangles are the low-rate (1/30 Hz) GPS stations. Red diamond is the strong motion station. The strong motion data are downloaded from the Center for Engineering Strong Motion Data (www.strongmotioncenter.org) and the high-rate and low-rate GPS data are from Wei et al. (2018). The black (observed) and red (kinematically synthetic) curves are the vertical waveforms adapted from Wei et al. (2018) at stations chlm, sndl, and KATNP, filtered between 0.02 and 0.33 Hz. The black and blue arrows denote the observed and kinematically simulated coseismic horizontal displacements at the GPS sites. The dots indicate relocated seismicity between 1995 and 2003. (b) Same as in (a), except for the coseismic slip, ground waveforms, and GPS displacements from the dynamic rupture simulation. The parameters for the dynamic model are $C = 20\%$, $B = 0.9$, and $S = 0.5$.

2. Method and Model Parameters

First, we calculate the coseismic stress drop $\vec{\Delta\tau}_{kin}$ of the 2015 Nepal earthquake basing on a kinematic model. It has been suggested that this event was confined at a relatively flat décollement that is bounded by steeper ramps (Hubbard et al., 2016; Qiu et al., 2016). To focus on the coseismic process, we consider a planar dip-slip fault with a dip angle of 7° embedded in an elastic domain, the velocity structure of which is approximated by a 1-D layer model (Table 2). A sufficiently large domain ($200 \times 260 \times 60$ km) is constructed to avoid the boundary effects. Free slip boundaries (no-slip in the direction normal to the boundaries) are applied on all sides of the domain except for the free surface. The kinematic slip model (Wei et al., 2018) is smoothed to eliminate traction singularities and cutoff at 1 m (Figure 1a). The calculated static stress drop, with both strike ($\Delta\tau_{str}$) and dip ($\Delta\tau_{dip}$) components (Figure 2), is also smoothed for the input of the dynamic models.

In the dynamic models, we apply a linear slip-weakening friction law on the fault, in which the friction coefficient f is given by

$$f(\delta) = \begin{cases} f_s - (f_s - f_d)\delta/d_0 & \delta \leq d_0 \\ f_d & \delta > d_0 \end{cases} \quad (1)$$

where f_s is the static friction coefficient, f_d is the dynamic friction coefficient, δ is the fault slip, and d_0 is the slip-weakening distance. We set up a constant effective normal stress $\sigma_n = 100$ MPa and an artificial constant f_d; thus, we have the dynamic friction $|\vec{\tau}_d| = f_d\sigma_n$, where $|\cdot|$ means the absolute value of stress. Here we set up the rake of $\vec{\tau}_d$ as 100°, same as the suggested rake of this event (Avouac et al., 2015).

We assume that the slip-weakening distance d_0 is linearly proportional to the observed kinematic slip as suggested by previous seismic observations (Tinti et al., 2005; Viesca & Garagash, 2015), i.e., $d_0 = Cu_{kin}$ where u_{kin} is the slip from the kinematic model (Figure 1a) and C is a free parameter. The cases with uniform d_0 are also considered. The initial shear stress is $\vec{\tau}_0 = B\vec{\Delta\tau}_{kin} + \vec{\tau}_d$, where $\vec{\Delta\tau}_{kin}$ is the static stress drop calculated from the kinematic model (Figure 2) and B is another free parameter. The stress drop of the dynamic model is $\vec{\Delta\tau}_{dyn} = \vec{\tau}_0 - \vec{\tau}_f$. It is noted that

Table 1
Estimated Rupture Parameters of the 2015 Nepal Gorkha M_w7.8 Earthquake

Total moment (10^{20} N m)	Rupture speed (km/s)	Duration (s)	Rise time (s)	References
7.2	2.8 ± 0.3	45–55		Avouac et al. (2015)
	2.9	~55		Fan & Shearer (2015)
	3.3	65	~6	Galetzka et al. (2015)
7.7	3.1–3.3	50		Grandin et al. (2015)
9.63–7.87	3	50–60	4–6	Lay et al. (2016), Liu et al. (2016), Wang & Mori (2016), Wei et al. (2018), and Yagi & Okuwaki (2015)
	2.7			Meng et al. (2016)
9.09	3.3	50–55		He et al. (2015)
6.4	3.2	50–60	8–10	Yue et al. (2016)
6.4–9.6	3 ± 0.2	47–53	4–8	Summary

Table 2
The 1-D Velocity Model Used in This Paper

Thickness (km)	V_S (km/s)	V_P (km/s)	Density (g/cm^3)
4.0	3.20	5.50	2.53
12.0	3.40	5.85	2.64
4.0	3.50	6.00	2.69
6.5	3.70	6.45	2.83
10.0	3.85	6.65	2.90
5.0	4.15	7.20	3.07
14.0	4.20	7.50	3.17

the residual stress $|\vec{\tau_f}|$ rarely equals to $|\vec{\tau_d}|$ in the dynamic rupture models, and we call it overshoot for $|\vec{\tau_f}| < |\vec{\tau_d}|$ and undershoot for $|\vec{\tau_f}| > |\vec{\tau_d}|$. The scalar fault strength is set as $\tau_s = f_s\sigma_n = (1 + S)(|\vec{\tau_0}| - |\vec{\tau_d}|) + |\vec{\tau_d}|$, where S is the nondimensional seismic ratio. In order to obtain the first-order information, C, B, and S are set as uniform constants on the entire seismogenic fault, which correspond to d_0, initial shear stress, and strength drop, respectively.

We use PyLith (Aagaard et al., 2013) to conduct the dynamic rupture simulations. The rupture is initiated from the U.S. Geological Survey epicentral location (http://earthquake.usgs.gov/earthquakes/eventpage/us20002926) by a time-weakening scenario with a constant rupture speed of half of the S wave speed, which can transfer to slip-weakening scenario spontaneously. The absorbing boundary condition (Aagaard et al., 2013) is applied on all boundaries except for the free surface. We set the grid size and time step to be 250 m and 0.01 s, respectively, meeting the minimum requirement of the cohesive zone size (Supporting information). We test the resolution by reducing the grid size to 150 m for the best fit model and find the effects of grid size are minor, showing that our selection of grid size 250 m does not affect the model results.

3. Results

3.1. Constraint From Kinematic Source Parameters

Because of the strong trade-offs among frictional parameters and initial shear stress, we conduct a large number of simulations in which C is changed from 10 to 60% (i.e., average slip-weakening distance $\overline{d_0}$ from 0.3 to 1.8 m), B is changed from 0.7 to 1.2, and S is changed from 0.1 to 1.5. We first investigate the trade-off patterns of final seismic moment of the dynamic models. Given the same initial shear stress, we find that final seismic moment increases with the slip-weakening distance d_0 for $C < 30\%$ and decreases for $C > 30\%$, but always decreases with strength drop (Figure 3a). Unsurprisingly, final seismic moment increases with initial shear stress monotonously for all values of d_0 and strength drop (Figure 3c). For static analysis, the final seismic moment can be uniquely determined by the initial and final shear stress given the dimension of the seismogenic fault (Aki, 1972). However, it also depends on the frictional parameters in dynamic models
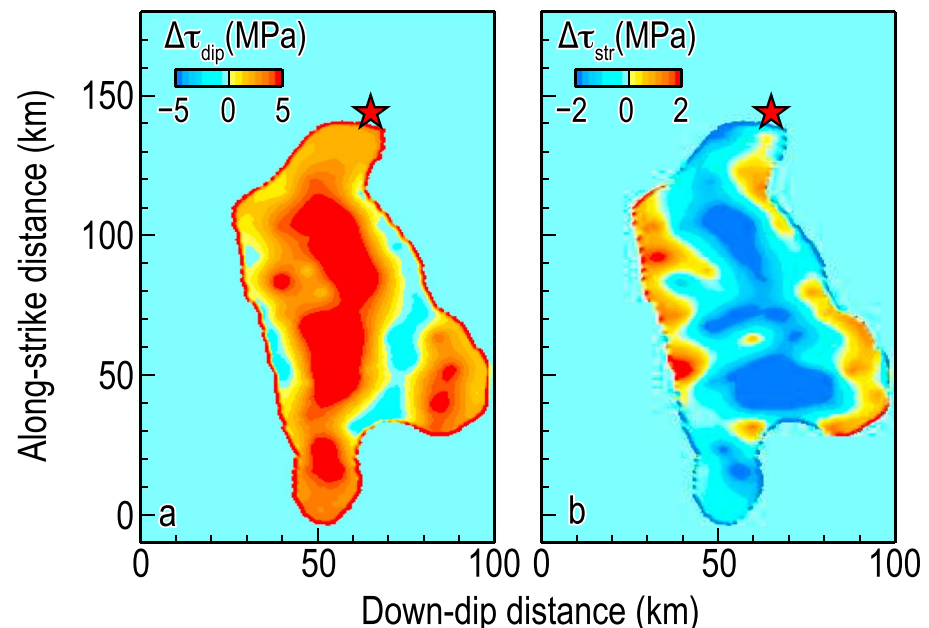
Figure 2. (a) Downdip and (b) along-strike static stress drops calculated from the kinematic slip model. Red stars mark the hypocenter of the main shock.
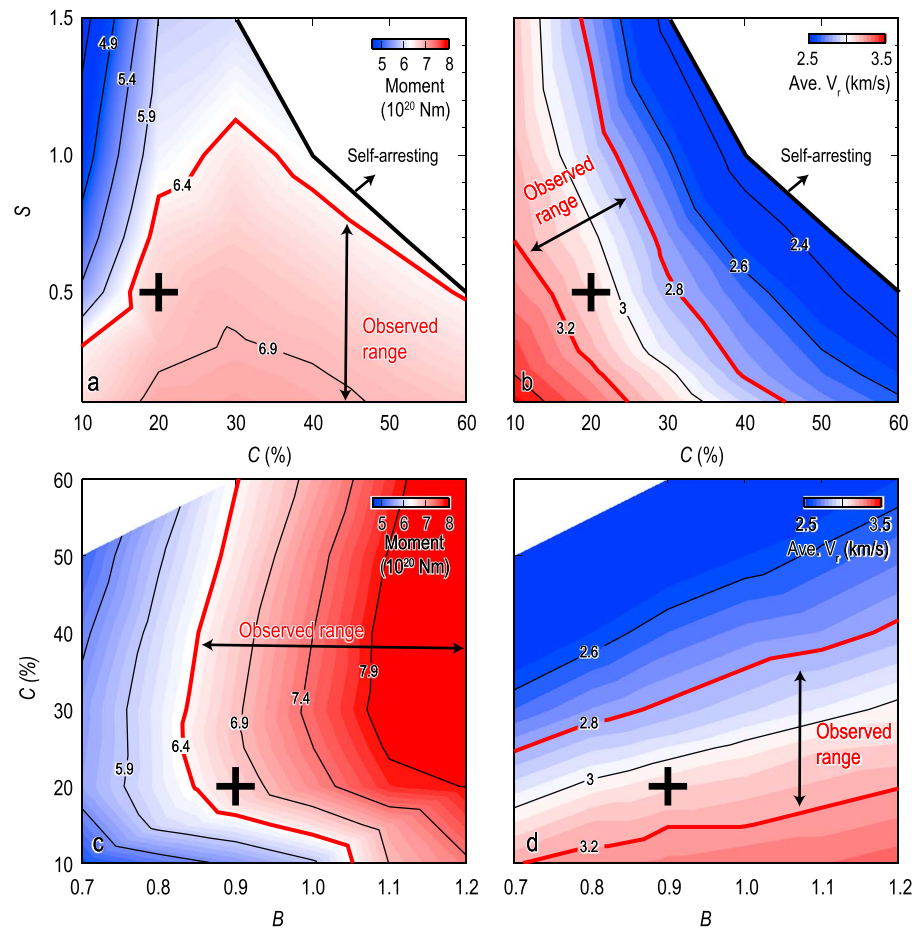
Figure 3. Trade-off patterns of seismic moment and rupture speed. Dependencies of (a and c) seismic moment and (b and d) rupture speed on C (d_0), S (strength drop), and B (initial shear stress). For a and b, $B = 0.9$, and for c and d, $S = 0.5$. The thick red curves mark the observed ranges of seismic moment and rupture speed, respectively. The black thick *cross* indicates the best fit dynamic model. Thick black curves show the critical boundaries that separate breakaway and self-arresting ruptures given the same nucleation condition.

so that we cannot determine the frictional parameters and initial shear stress of dynamic model solely from the kinematically inverted seismic moment, because of the trade-offs.

We also compare the rupture speeds of the dynamic models with those estimated from the kinematic source models and backprojection methods (Table 1). The average rupture speed (average value along the central depth of the seismogenic fault) decreases with d_0 and strength drop monotonously (Figure 3b), but increases with initial shear stress (Figure 3d). Although the observed range of rupture speed defines a suitable region of model parameters, there are clear trade-offs among the strength drop, d_0, and the initial stress. We also cannot uniquely determine the frictional parameters and initial shear stress solely from the rupture speed.

However, the trade-off patterns of seismic moment and rupture speed show distinctly different trends (Figure 3), making it feasible to combine these two kinds of observations to reduce the trade-offs. If we super-impose the trade-off pattern of rupture speed on that of final seismic moment, the observed seismic moment (6.4–9.6 × 10^{20} Nm; Table 2) and rupture speed (3 ± 0.2 km/s; Table 2) can roughly enclose a region with C between 10 and 40%, S between 0.1 and 1.0, and B between 0.8 and 1.2 (Figure 3). It is noted that when the slip-weakening distance d_0 and strength drop are larger than certain critical values (thick black curves in Figure 3), the ruptures become self-arresting and cannot rupture the entire seismogenic fault, which is mainly controlled by the energy balance between strain energy release and the fracture energy (Weng & Yang, 2017).
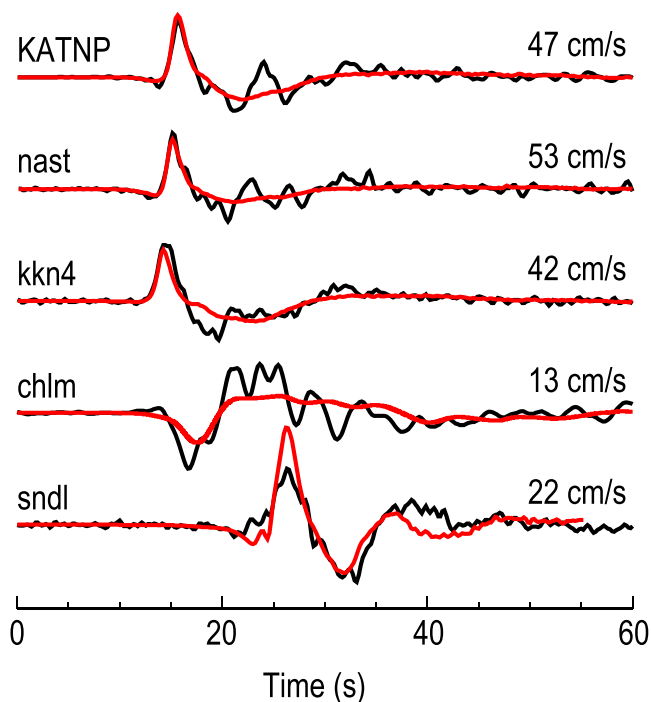
Figure 4. The black and red curves are the observed and the synthetic vertical waveforms (0.02–1, 0.02–0.3 Hz for station chlm) from the best fit dynamic model with $C = 20\%$, $B = 0.9$, and $S = 0.5$. The amplitudes of the waveforms are indicated on the top right of each observed waveform.

3.2. Constraint From Near-Field Observations

In addition to the constraints from seismic moment and rupture speed, we make further efforts to shrink the range of the best solution by using near-field seismic and geodetic observations. We first compare our near-field synthetic ground velocities with the measurements at four high-rate (5 Hz) cGPS stations kkn4, nast, chlm, and sndl, and one strong motion station KATNP (Figure 1 and Movie S1). Due to the resonance effects of the Kathmandu basin on the horizontal components of waveforms (Galetzka et al., 2015), only the vertical waveforms are considered here. Both the observed and synthetic data are transformed to velocities, filtered between 0.02 and 1 Hz, and aligned by the time of their peak velocities (Figure 4). Several factors in our dynamic model may affect the peak arrivals: the artificial nucleation speed, the velocity structure, and fault geometry etc. Tuning the artificial nucleation speed can change the alignments of all waveforms by a constant time shift. But there are still offsets of 1–3 s between the synthetic and observed waveforms after this constant time shift, which could attribute to the simple velocity structure and fault geometry we used.

In general, our synthetics show good agreement with the data. The secondary pulses with smaller amplitude at the stations KATNP, nast, and chlm are likely caused by the second-order effects, such as 3-D velocity structure (Galetzka et al., 2015) or fault geometries (Hubbard et al., 2016; Qiu et al., 2016). We quantify the least squares misfit functions between the synthetic and observed waveforms. The waveforms appear to be sensitive to d_0 and d_0 could be bounded near $C = 20\%$ (Figures 5a and 6a). But both strength drop and initial stress still suffer trade-offs (Figures 5a and 5c). We further test the sensitivity of the waveforms on the frictional parameters and find that the synthetic waveform is more sensitive to the d_0 than to the S ratio (Figure 6).

Since static ground displacement is more sensitive to the final seismic moment than to the moment rate, we also compare our modeled ground displacements with the static GPS measurements (Figure 1). The least squares misfit functions of three-component static displacements also show significant trade-offs (Figures 5b and 5d). However, the trade-off trends are distinctly different from those of seismic waveforms, especially between d_0 and the initial shear stress (Figures 5c and 5d). Thus, we define a total misfit function to combine the constraints from both seismic waveforms and static GPS displacements, for example, average of these two misfit functions with equal weighting, except for the station sndl that is weighted by half due to its further distance. As shown in Figure 7, the best solution of the model parameters is well bounded by the total misfit, such as $C = 20\%$ (corresponding to $\overline{d_0} \simeq 0.6$ m), $B = 0.9$, and $S = 0.5$. The synthetic ground velocities and displacements of this best fit dynamic model are well consistent with the near-field observations (Figure 1b).

4. Discussion

4.1. Comparison With Kinematic Models

Because a hypothetical uniform d_0 has been commonly used on seismogenic fault in previous dynamic simulations (Ma et al., 2008; Olsen et al., 1997; Weng et al., 2015, 2016; Yang et al., 2013), we then test the cases with uniform d_0. In these cases, d_0 is changed from 0.3 to 2.4 m while fixing $B = 0.9$, and $S = 0.5$. We can obtain a similar best fit dynamic model with a uniform $d_0 = 0.9$ m (Figure 8). As the misfit of the best fit model with slip-scaled d_0 is smaller than those with uniform d_0 (Figure 8), we conclude that the average slip-weakening distance $\overline{d_0}$ of this event is 0.6 ± 0.3 m. This value is much smaller than the kinematical estimation of ~5 m by Galetzka et al. (2015). In addition, it appears that the peak slip rate of our best fit dynamic model is nearly 6 m/s (Figure 9b), greater than the kinematically obtained value, 1.1 m/s (Galetzka et al., 2015). We find that the spatial width of slip pulse along strike is ~20 km in their kinematic model
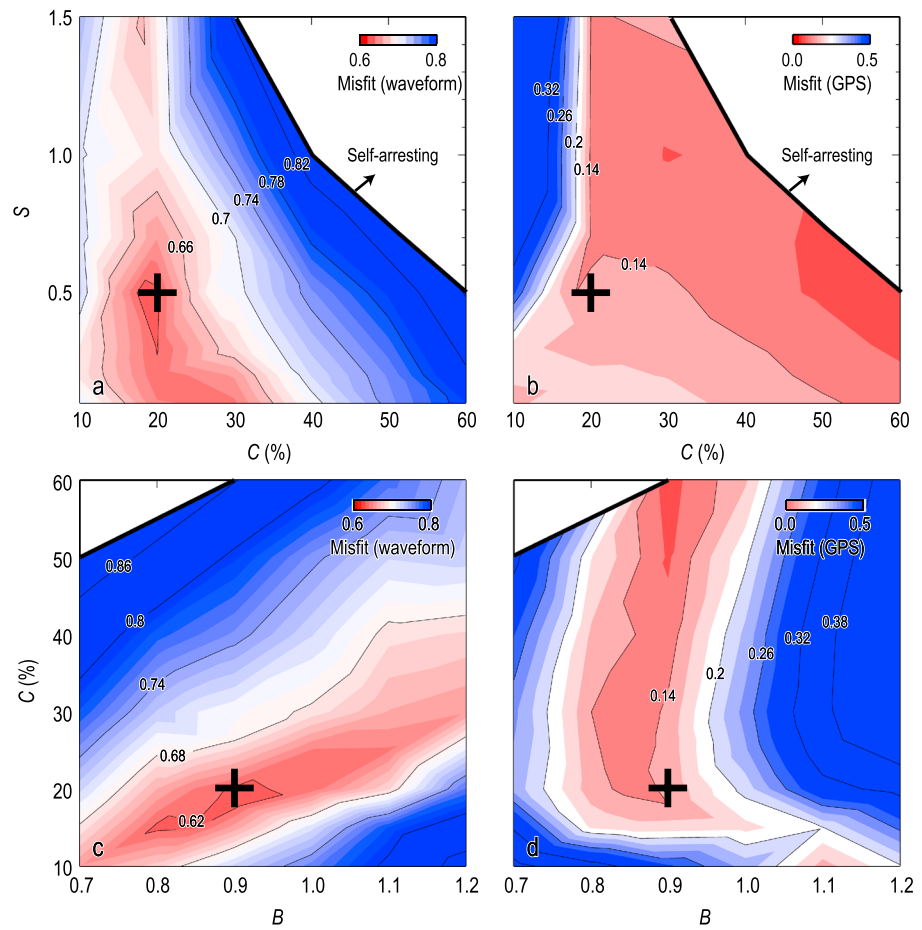
Figure 5. Dependencies of misfit functions of (a and c) waveforms and (b and d) GPS data on C (d_0), S (strength drop), and B (initial stress) of the dynamic models. For a and b, $B = 0.9$ and for c and d, $S = 0.5$. The black thick *cross* indicates the best fit dynamic model.
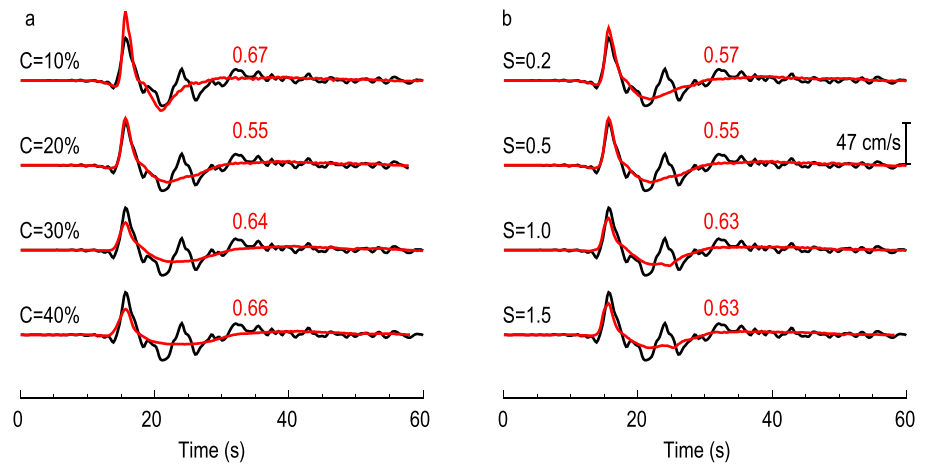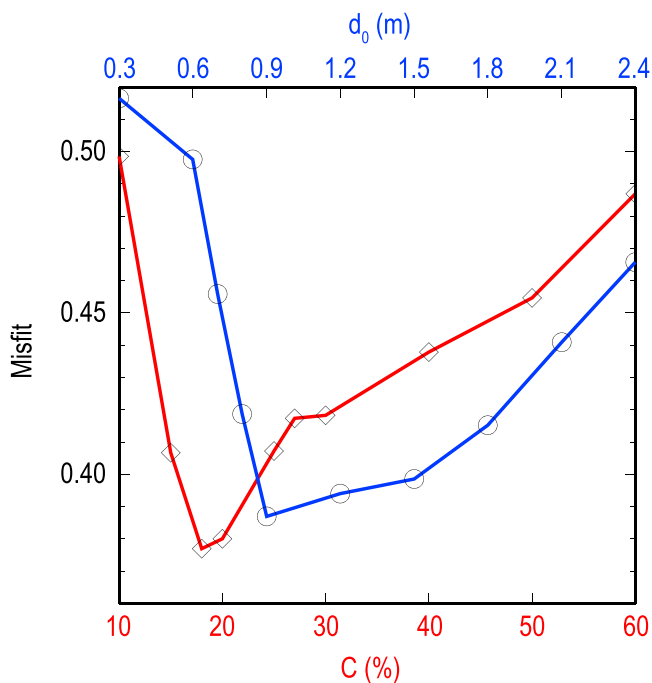

Figure 6. (a) The black and red curves are the observed and synthetic vertical waveforms at strong motion station KATNP (0.02–1 Hz). The synthetic vertical waveforms are extracted from the dynamic models with $S = 0.5$, $B = 0.9$, and different C shown in the legend. (b) For the dynamic models with $B = 0.9$, $C = 20\%$, and different S shown in the legend. Red texts show the least-square misfits of the waveform pairs.
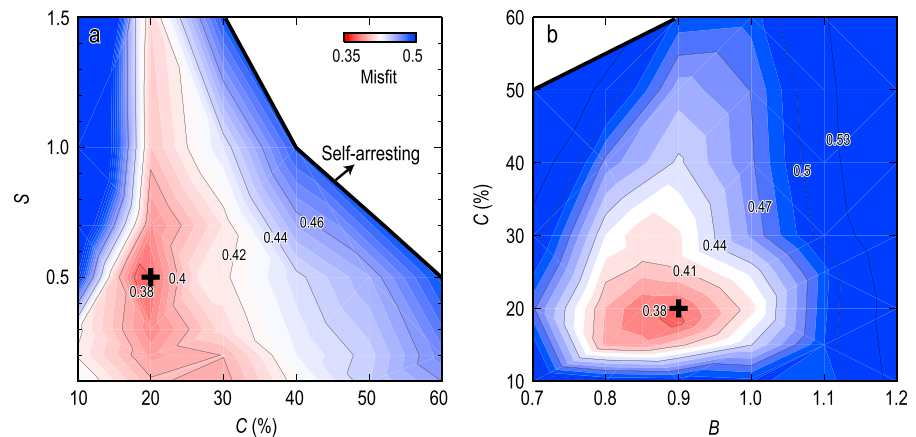
Figure 7. (a) Contours show the total misfit value, including waveforms and GPS displacements, as a function of C (d_0) and S (strength drop). $B = 0.9$. The trade-offs are well removed in the total misfit functions. (b) Total misfit as a function of C and B. $S = 0.5$.

(Galetzka et al., 2015), much larger than that in our dynamic model that is highly variable and mainly concentrates near the rupture front (Figure 10). The kinematic methods likely smear the narrow and strong slip pulse to a wider region, and thus overestimate the d_0 even a dynamical-like regularized Yoffe function was used (Galetzka et al., 2015). In our model, there is a narrow high slip-rate pulse separating from the main pulse after 120 km along-strike propagation, which may be caused by re-rupturing of certain fault segment (Figure 10 and Movie S1). In company with such re-rupturing, there exist localized supershear speeds, as observed in all dynamic models (Figure 9a). Since the rupture mode of this event is mostly mode III, we expect that the entire fault will have sub-shear rupture speeds. However, due to heterogeneous properties and stresses, some locations could have mixed modes and thus have supershear speed, even for the case with $S = 1.5$.

To analyze the slip rate function, we track three parameters of slip rate function in our dynamic models using the definitions of the regularized Yoffe function, such as peak slip rate $\dot{u}_p$, risetime t_{ris}, and process-zone time t_p (Figure 11a). The risetime t_{ris} is defined as the period from when the slip rate first reaches 0.01 m/s to when the slip reaches 90% of the final slip. The process-zone time t_p is defined as the time beginning when the slip rate first reaches 0.01 m/s and ending at peak slip rate $\dot{u}_p$. We find that the average peak slip rate $\dot{u}_p$ decreases with d_0, while the average risetime t_{ris} and the average process-zone time t_p both increase with d_0. In contrast, the three slip rate function parameters weakly depend on strength drop. The estimation of risetime of the 2015 M_w7.8 Nepal earthquake from several kinematic models is approximately 4–8 s (Table 1). Though the definition of risetime in these kinematic models is different from that in our dynamic models, the average value of the risetime is consistent with our best fit dynamic model. In the best fit dynamic model, the average t_p is smaller than 1 s and the average $\dot{u}_p$ is larger than 3 m/s (Figure 11).

4.2. Energy Budget of the 2015 Nepal Gorkha Earthquake

The total fracture energy of the best fit dynamic model is $G_C = \frac{1}{2}\overline{\tau_s - \tau_d}\;\overline{d_0}$

Figure 8. The red curve is the total misfits as a function of C, and blue curve is the total misfits as a function of d_0. $B = 0.9$ and $S = 0.5$. The best fit C is 20% corresponding to $\overline{d_0} = 0.6$ m and the best fit uniform d_0 is 0.9 m.

$A \approx 0.9 \times 10^{16}$ J ($\overline{\tau_s - \tau_d} \approx 4.8$ MPa, $\overline{d_0} = 0.6$ m, rupture area $A = 6 \times 10^3$ km^2). The overshoot of this model is about 20%, similar with a circular rupture that has overshoot between 15 and 20% when the rupture speed is between 0.6 and 0.9 V_S (Madariaga, 1976). Considering the total released strain energy of the best fit dynamic model with overshoot (Kanamori &
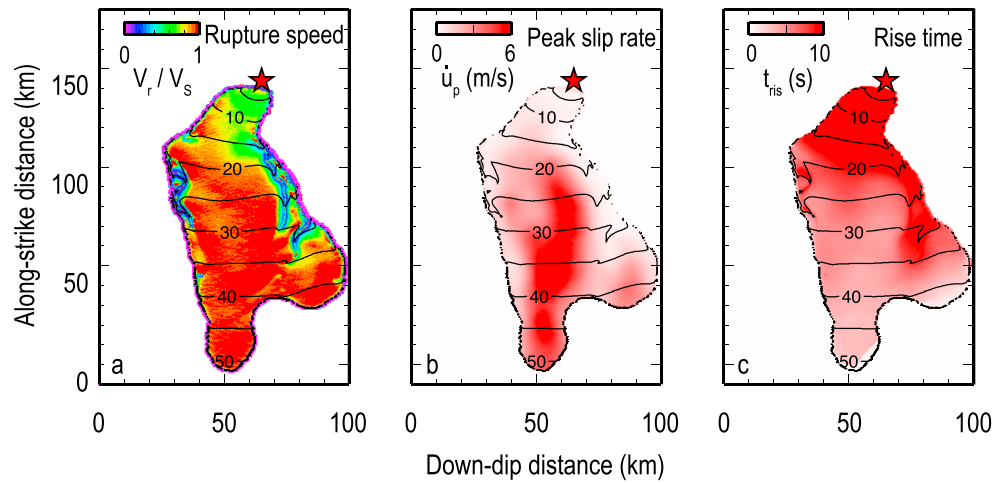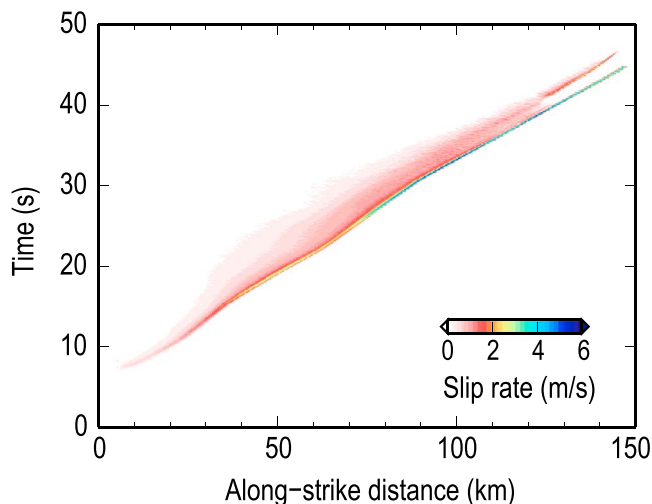
Figure 9. Rupture details of the dynamic model. (a) The rupture speed (normalized by the S wave velocity), (b) the peak slip rate, and (c) the risetime distributions of the dynamic model with C = 20%, B = 0.9, and S = 0.5. The contours mark the rupture fronts in every 5 s.

Rivera, 2006), $\Delta W = \frac{1}{2}\overline{\tau_0 - \tau_f}\ \overline{u}A - \overline{\tau_d - \tau_f}\overline{u}A \approx 2.3 \times 10^{16}$ J ($\overline{\tau_0 - \tau_f} \approx 3.9$ MPa, $\overline{u} \approx 3$ m, $\overline{\tau_d - \tau_f} = 0.7$ MPa), the estimated radiated energy is approximated as $E_R = \Delta W - G_C \approx 1.4 \times 10^{16}$ J, which agrees with the estimations by integrating the source spectrum, $1 \times 10^{16} - 6 \times 10^{16}$ J (Denolle et al., 2015; Lay et al., 2016). The average fracture energy per unit area is $\overline{G_C} \approx 1.4 \times 10^6$ J/m^2, 1 order of magnitude smaller than the expected value from the slip-fracture energy scaling (slip ~3 m) that is ~3×10^7 J/m^2 (Viesca & Garagash, 2015), but is well consistent with the estimated values, on the order of 10^6 J/m^2, from the dynamic models for the 1992 Landers, 2000 Tottori, and 1995 Kobe events (Mikumo et al., 2003; Olsen et al., 1997). The deviation may stem from the different values of d_0 from the dynamic and kinematic models, which also highlight the importance of using dynamic rupture model for determining the friction parameters.
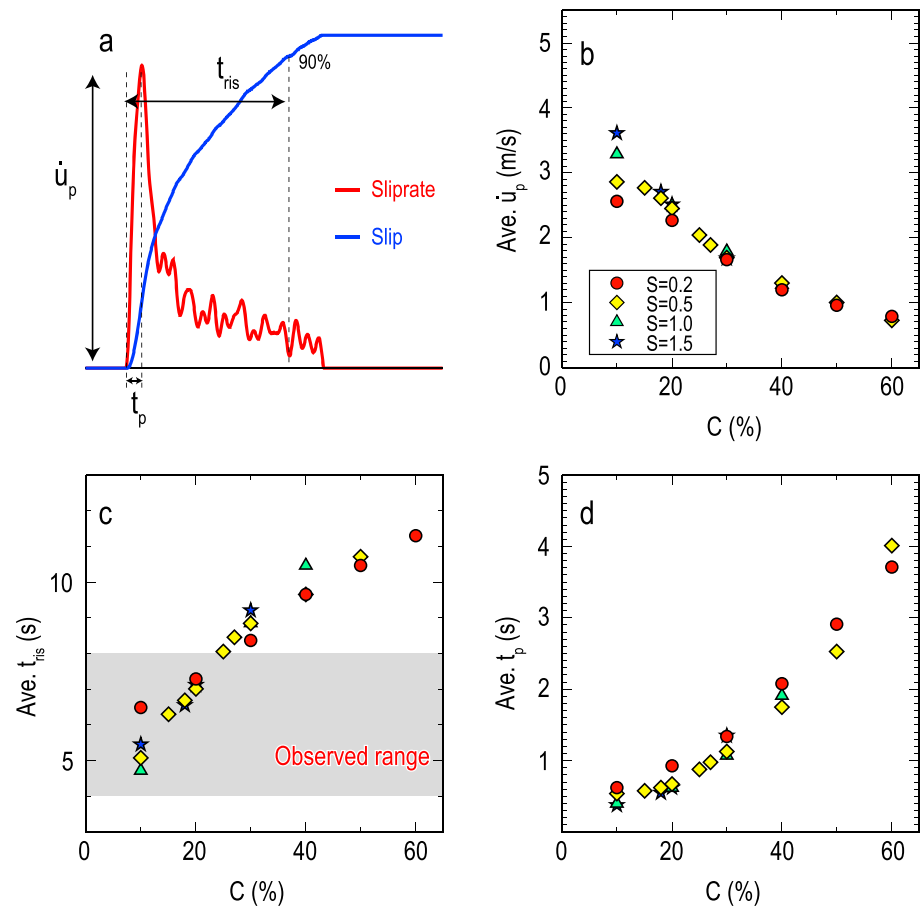
4.3. Sensitivity of Waveform

We also test the cases with $d_0 = 5$ m and find that the rupture can propagate only when S is close to zero (fault strength is close to initial shear stress). However, the amplitudes of ground waveforms are quite small in such extreme cases. Figure 12 shows that the waveform misfit is sensitive to the fracture energy when the fracture energy is larger than 1.4×10^6 J/m^2; for example, the contours of waveform misfit have similar trend with the fracture energy contours. In contrast, if the slip-weakening rate $\overline{(\tau_s - \tau_d)/d_0} > 10$ MPa/m, the waveform misfit is sensitive to the slip-weakening rate. The fracture energy and slip-weakening rate of the extreme model with $d_0 = 5$ m (S~0.0) are ~8×10^6 J/m^2 and ~0.6 MPa/m, making it difficult to fit the near-field observations (Figure 12). The slip-weakening rate in the field may vary with slip if dynamic weakening mechanism occurs (Rice, 2006; Wibberley & Shimamoto, 2005). But the order of magnitude of d_0 is estimated to be 0.5 m given the average risetime of ~6 s, according to Rice (2006, equation (29)) that relates d_0 and risetime basing on a thermal pressurization model.

Although we use an artificial constant f_d in this paper, our tests show that the absolute value of f_d is not important, as the synthetics produced from different f_d values are indistinguishable (Figure 13a). The difference between the static and the dynamic frictional stress in the slip-weakening friction law (i.e., strength drop) is more important than the absolute level of the dynamic frictional stress. As we use both dip and strike


Figure 10. Slip rate history at the central depth of the fault in the dynamic model with C = 20%, B = 0.9, and S = 0.5.

Figure 11. (a) Slip and slip rate function (SRF) with the definition of the peak slip rate $\dot{u}_p$, risetime t_{ris}, and process zone time t_p on the fault. (b–d) The dependencies of three important parameters (average values) of THE SRF on C and S. Different colored symbols mark different S shown in the legend. Gray region in (c) shows the observed range of risetime (Table 1).

components of the kinematically inverted stress drop $\vec{\Delta\tau}_{kin}$ (Figure 2) to set up the initial shear stress, the rake of $\vec{\tau}_d$ needs to be considered. Our tests show that the rake of $\vec{\tau}_d$ has minor effects on the synthetic waveforms. This also holds true for the horizontal waveforms (Figure 14). The change of rake may slightly affect the amplitudes of horizontal waveforms by acting on the radiation pattern. The rake of $\vec{\tau}_d$ can affect the orientation of static GPS displacements (Figure 13b), which shows that considering two components of initial shear stress is necessary. In this study, the rake of $\vec{\tau}_d$ is set up according to the observed value of this event. In calculating the static stress drop from the kinematic slip, we artificially cut off the slip less than 1 m for two reasons: the smaller slip of < 1 m has lower reliability for an M_w7.8 event and the effects of the cutoff value on the waveforms and static displacements are minor (Figure 13c).

We note that the waveform fits of our dynamic models for horizontal components are not as good as the vertical components (Figures 4 and 14). The waveform fits at station sndl are better than another four stations. The observed horizontal waveforms at KATNP and nast stations have larger amplitudes and more peaks than the synthetic waveforms (Figure 14). This deviation may be caused by the 3-D sedimentary structure in the Kathmandu Valley (Galetzka et al., 2015; Wei et al., 2018). A 3-D velocity model may improve the horizontal waveform fits (Wei et al., 2018), and could be applied to the dynamic models in the future.

4.4. Factors Not Considered

Several factors that could affect the estimations of d_0 were not considered in this study, such as geometrical roughness of fault, inelastic material properties, and different friction models. Irregular fault geometry could affect the rupture propagation and thus the ground waveforms (e.g., Wang et al., 2017; Yu et al., 2018). Here
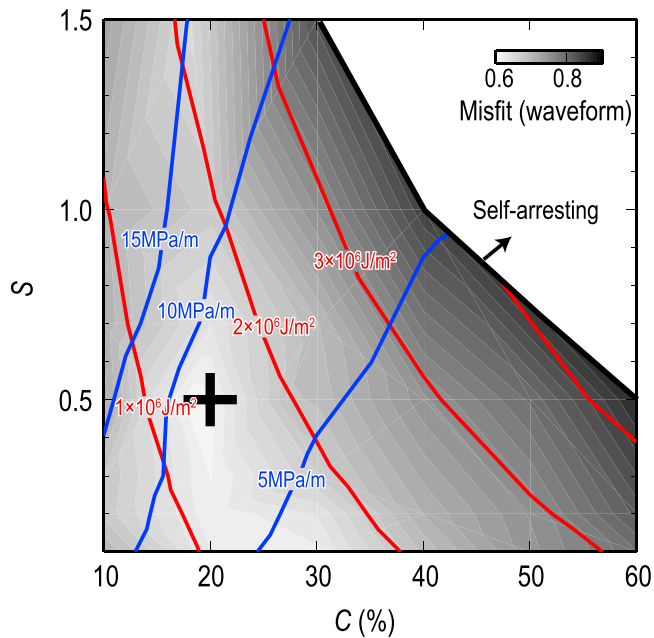
Figure 12. Misfit function of waveforms on C and S, same as Figure 5a. The red curves are the contours of average fracture energy of the dynamic models. The blue curves are the contours of average slip weakening rate of the dynamic models, $\overline{(\tau_s - \tau_d)/d_0}$.

we used planar fault geometry as suggested by Hubbard et al. (2016). Another reason for us to use the simple fault geometry is to compare our dynamic model results with the kinematic model, which was obtained on a planar fault (Wei et al., 2018).

The rupture tips carrying highly concentrated stress may cause off-fault yielding and weaken the near-field waveforms (Ma, 2012). Off-fault yielding during earthquakes may generate damage fault zones that have been observed in a number of crustal faults (e.g., Yang, 2015; Yang et al., 2011, 2014; Yang & Zhu, 2010) and are suggested to significantly modulate rupture propagation (e.g., Weng et al., 2016). Ignoring the off-fault yielding might lead to overestimate the actual d_0. Applying inelastic materials in dynamic models (Andrews, 2005) could be implemented in future investigations if off-fault yielding at seismogenic depths can be reasonably constrained.

Moreover, the slip-weakening friction law used in this study is a specified and simplified friction law. Although our dynamic model constrains the best fit model with $S = 0.5$, but the simple friction law may not capture the very early evolution of friction, such as the flash heating that may largely reduce the friction coefficient during very small slip (Rice, 2006). Applying a more complicated friction model, such as including dynamic weakening effects, may better depict the frictional behavior of faults (Rice, 2006). Despite the above limitations and uncertainties, the method developed in this study could be applicable to other events and provide insights of earthquake physics.
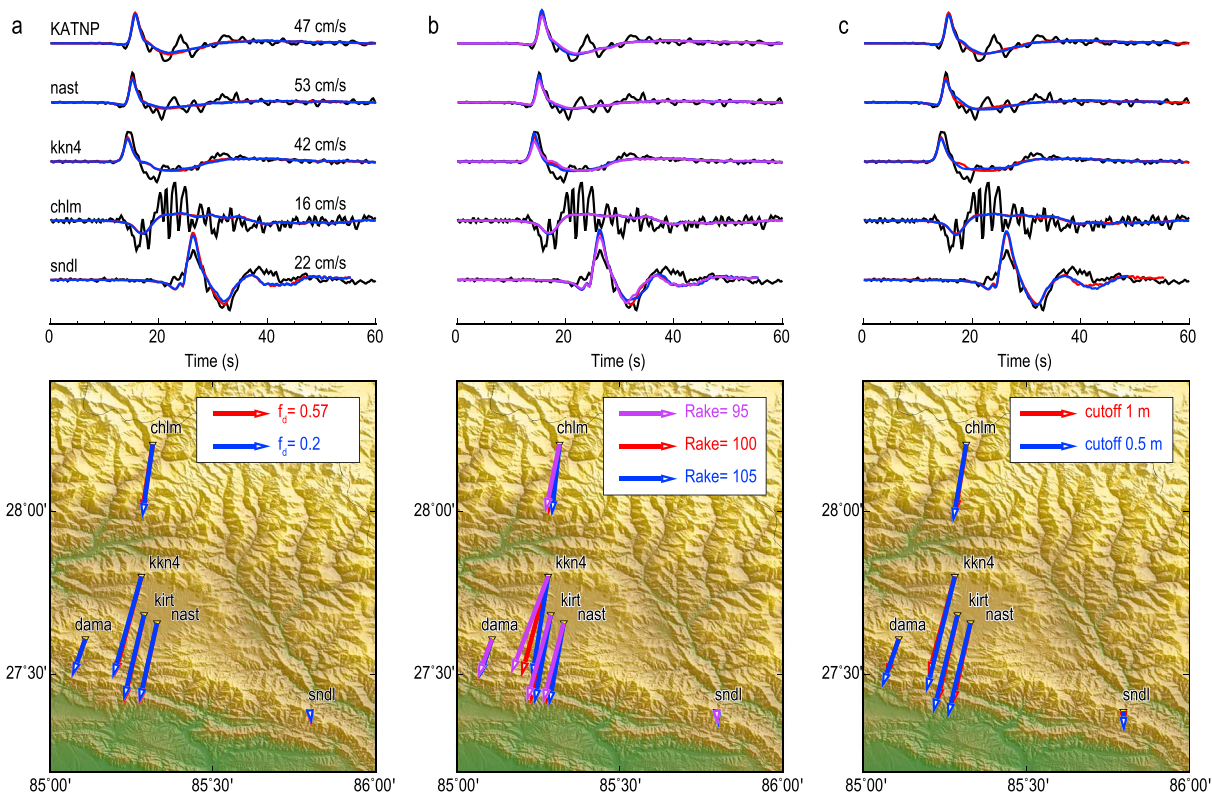
Figure 13. Comparison of (top) waveforms and (bottom) GPS displacements for different (a) dynamic friction coefficients f_d, (b) rake angles of $\vec{\tau_d}$, and (c) cutoff slip.
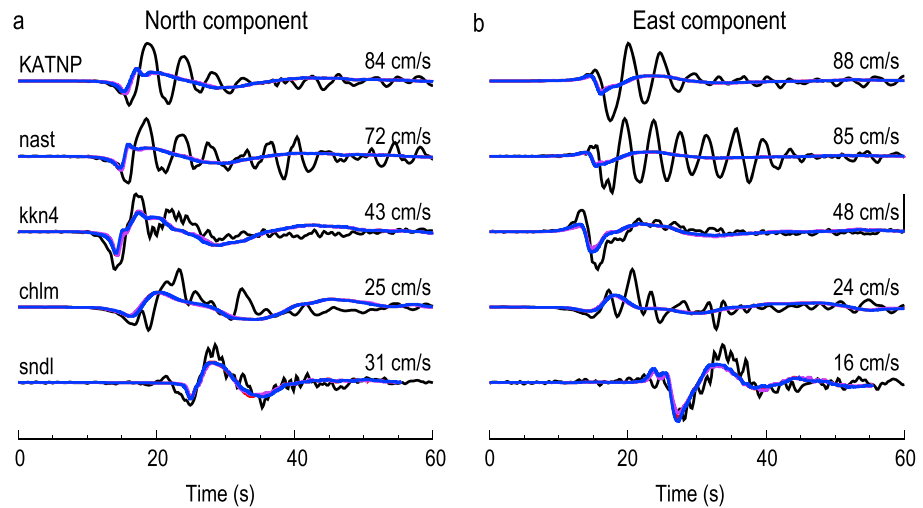
Figure 14. The black and red curves are the observed and the synthetic horizontal waveforms (0.02–1 Hz) from the best fit dynamic model. The blue and purple curves are synthetic horizontal waveforms with different rake angles of $\vec{\tau}_d$ (i.e., 95° and 105°), respectively. (a) North-south component. (b) East-west component. The band-pass filter for the station chlm is 0.02–0.33 Hz. The amplitudes of the normalized waveforms are indicated on the top right of each observed waveform.

5. Conclusion

Here we demonstrate that by integrating constraints from kinematic source models and near-field observations, we can determine the critical slip-weakening distance d_0 and strength drop on seismogenic faults. In the case of the 2015 Nepal M_w7.8 earthquake, we find that the seismic moment, rupture speed, and misfit of near-field waveforms and static GPS displacements show distinctly different trade-off patterns, controlled by the rupture dynamics. Combining the different lines of observations helps to remove the trade-off between frictional parameters and initial stress. The best fit dynamic model yields a d0 value of ~0.6 m and an average fracture energy $\overline{G_C} \simeq 1.4 \times 10^6$ J/m² for the 2015 M_w7.8 Gorkha, Nepal earthquake. The well-constrained frictional parameters could be used for future dynamic models to estimate the ground motion, such as the peak ground velocity or peak ground acceleration that is important for assessing seismic hazard. Similar approach could also be conducted for other great earthquakes, enabling broad estimations of the dynamic source parameters in global perspectives that can better reveal the intrinsic physics of earthquakes.

References

Aagaard, B., Knepley, M., & Williams, C. (2013). A domain decomposition approach to implementing fault slip in finite-element models of quasi-static and dynamic crustal deformation. *Journal of Geophysical Research: Solid Earth*, *118*, 3059–3079. https://doi.org/10.1002/jgrb.50217

Aki, K. (1972). Earthquake mechanism. *Tectonophysics*, *13*(1–4), 423–446. https://doi.org/10.1016/0040-1951(72)90032-7

Andrews, D. (2005). Rupture dynamics with energy loss outside the slip zone. *Journal of Geophysical Research*, *110*, B01307. https://doi.org/10.1029/2004JB003191

Avouac, J.-P., Meng, L., Wei, S., Wang, T., & Ampuero, J.-P. (2015). Lower edge of locked Main Himalayan Thrust unzipped by the 2015 Gorkha earthquake. *Nature Geoscience*, *8*, 708. https://doi.org/10.1038/ngeo2518, https://www.nature.com/articles/ngeo2518#supplementary-information

Dalguer, L., Irikura, K., & Riera, J. (2003). Generation of new cracks accompanied by the dynamic shear rupture propagation of the 2000 Tottori (Japan) earthquake. *Bulletin of the Seismological Society of America*, *93*(5), 2236–2252. https://doi.org/10.1785/0120020171

Denolle, M. A., Fan, W., & Shearer, P. M. (2015). Dynamics of the 2015 *M*7.8 Nepal earthquake. *Geophysical Research Letters*, *42*, 7467–7475. https://doi.org/10.1002/2015GL065336

Di Toro, G., Han, R., Hirose, T., De Paola, N., Nielsen, S., Mizoguchi, K., et al. (2011). Fault lubrication during earthquakes. *Nature*, *471*(7339), 494–498. https://doi.org/10.1038/nature09838

Dunham, E. M., & Archuleta, R. J. (2004). Evidence for a supershear transient during the 2002 Denali fault earthquake. *Bulletin of the Seismological Society of America*, *94*(6B), S256–S268. https://doi.org/10.1785/0120040616

Fan, W., & Shearer, P. M. (2015). Detailed rupture imaging of the 25 April 2015 Nepal earthquake using teleseismic P waves. *Geophysical Research Letters*, *42*, 5744–5752. https://doi.org/10.1002/2015GL064587

Fukuyama, E., & Mikumo, T. (2007). Slip-weakening distance estimated at near-fault stations. *Geophysical Research Letters*, *34*, L09302. https://doi.org/10.1029/2006GL029203

Galetzka, J., Melgar, D., Genrich, J. F., Geng, J., Owen, S., Lindsey, E. O., et al. (2015). Slip pulse and resonance of the Kathmandu basin during the 2015 Gorkha earthquake, Nepal. *Science*, *349*(6252), 1091–1095. https://doi.org/10.1126/science.aac6383

Goto, H., & Sawada, S. (2010). Trade-offs among dynamic parameters inferred from results of dynamic source inversion. *Bulletin of the Seismological Society of America*, *100*(3), 910–922. https://doi.org/10.1785/0120080250

Grandin, R., Vallée, M., Satriano, C., Lacassin, R., Klinger, Y., Simoes, M., & Bollinger, L. (2015). Rupture process of the M_w = 7.9 2015 Gorkha earthquake (Nepal): Insights into Himalayan megathrust segmentation. *Geophysical Research Letters*, *42*, 8373–8382. https://doi.org/10.1002/2015GL066044

Guatteri, M., & Spudich, P. (2000). What can strong-motion data tell us about slip-weakening fault-friction laws? *Bulletin of the Seismological Society of America*, *90*(1), 98–116. https://doi.org/10.1785/0119990053

He, X., Ni, S., Ye, L., Lay, T., Liu, Q., & Koper, K. D. (2015). Rapid seismological quantification of source parameters of the 25 April 2015 Nepal earthquake. *Seismological Research Letters*, *86*(6), 1568–1577. https://doi.org/10.1785/0220150131

Hubbard, J., Almeida, R., Foster, A., Sapkota, S. N., Bürgi, P., & Tapponnier, P. (2016). Structural segmentation controlled the 2015 M_w 7.8 Gorkha earthquake rupture in Nepal. *Geology*, *44*(8), 639–642. https://doi.org/10.1130/G38077.1

Ida, Y. (1972). Cohesive force across the tip of a longitudinal-shear crack and Griffith's specific surface energy. *Journal of Geophysical Research*, *77*(20), 3796–3805. https://doi.org/10.1029/JB077i020p03796

Ide, S., & Takeo, M. (1997). Determination of constitutive relations of fault slip based on seismic wave analysis. *Journal of Geophysical Research*, *102*(B12), 27,379–27,391. https://doi.org/10.1029/97JB02675

Kanamori, H., & Rivera, L. (2006). Energy partitioning during an earthquake. In *Earthquakes: Radiated Energy and the Physics of Faulting, Geophysical Monograph Series* (Vol. 170, pp. 3–13). Washington, DC: American Geophysical Union. Retrieved from http://resolver.caltech.edu/CaltechAUTHORS:20110629-112907012

Kaneko, Y., Fukuyama, E., & Hamling, I. J. (2017). Slip-weakening distance and energy budget inferred from near-fault ground deformation during the 2016 M_w7. 8 Kaikōura earthquake. *Geophysical Research Letters*, *44*, 4765–4773. https://doi.org/10.1002/2017GL073681

Lavé, J., & Avouac, J.-P. (2000). Active folding of fluvial terraces across the Siwaliks Hills, Himalayas of central Nepal. *Journal of Geophysical Research*, *105*(B3), 5735–5770. https://doi.org/10.1029/1999JB900292

Lay, T., Ye, L., Koper, K. D., & Kanamori, H. (2016). Assessment of teleseismically-determined source parameters for the April 25, 2015 M_W 7.9 Gorkha, Nepal earthquake and the May 12, 2015 M_W 7.2 aftershock. *Tectonophysics*, *714-715*, 4–20. https://doi.org/10.1016/j.tecto.2016.05.023

Liu, C., Zheng, Y., Wang, R., Shan, B., Xie, Z., Xiong, X., & Ge, C. (2016). Rupture processes of the 2015 M_w 7.9 Gorkha earthquake and its M_w 7.3 aftershock and their implications on the seismic risk. *Tectonophysics*, *682*, 264–277. https://doi.org/10.1016/j.tecto.2016.05.034

Ma, S. (2012). A self-consistent mechanism for slow dynamic deformation and tsunami generation for earthquakes in the shallow subduction zone. *Geophysical Research Letters*, *39*, L11310. https://doi.org/10.1029/2012GL051854

Ma, S., Custodio, S., Archuleta, R. J., & Liu, P. (2008). Dynamic modeling of the 2004 M_w 6.0 Parkfield, California, earthquake. *Journal of Geophysical Research*, *113*, B02301. https://doi.org/10.1029/2007JB005216

Madariaga, R. (1976). Dynamics of an expanding circular fault. *Bulletin of the Seismological Society of America*, *66*(3), 639–666.

Meng, L., Zhang, A., & Yagi, Y. (2016). Improving back projection imaging with a novel physics-based aftershock calibration approach: A case study of the 2015 Gorkha earthquake. *Geophysical Research Letters*, *43*, 628–636. https://doi.org/10.1002/2015GL067034

Mikumo, T., Olsen, K. B., Fukuyama, E., & Yagi, Y. (2003). Stress-breakdown time and slip-weakening distance inferred from slip-velocity functions on earthquake faults. *Bulletin of the Seismological Society of America*, *93*(1), 264–282. https://doi.org/10.1785/0120020082

Mikumo, T., & Yagi, Y. (2003). Slip-weakening distance in dynamic rupture of in-slab normal-faulting earthquakes. *Geophysical Journal International*, *155*(2), 443–455. https://doi.org/10.1046/j.1365-246X.2003.02047.x

Nielsen, S. B., & Olsen, K. B. (2000). Constraints on stress and friction from dynamic rupture models of the 1994 Northridge, California, earthquake. *Pure and Applied Geophysics*, *157*(11), 2029–2046. https://doi.org/10.1007/PL00001073

Olsen, K., Madariaga, R., & Archuleta, R. (1997). Three-dimensional dynamic simulation of the 1992 Landers earthquake. *Science*, *278*(5339), 834–838. https://doi.org/10.1126/science.278.5339.834

Peyrat, S., & Olsen, K. (2004). Nonlinear dynamic rupture inversion of the 2000 western Tottori, Japan, earthquake. *Geophysical Research Letters*, *31*, L05604. https://doi.org/10.1029/2003GL019058

Qiu, Q., Hill, E. M., Barbot, S., Hubbard, J., Feng, W., Lindsey, E. O., et al. (2016). The mechanism of partial rupture of a locked megathrust: The role of fault morphology. *Geology*, *44*(10), 875–878. https://doi.org/10.1130/G38178.1

Rice, J. R. (2006). Heating and weakening of faults during earthquake slip. *Journal of Geophysical Research*, *111*, B05311. https://doi.org/10.1029/2005JB004006

Sapkota, S. N., Bollinger, L., & Perrier, F. (2016). Fatality rates of the M_w ~8.2, 1934, Bihar-Nepal earthquake and comparison with the April 2015 Gorkha earthquake. *Earth, Planets and Space*, *68*(1), 40. https://doi.org/10.1186/s40623-016-0416-2

Tinti, E., Bizzarri, A., Piatanesi, A., & Cocco, M. (2004). Estimates of slip weakening distance for different dynamic rupture models. *Geophysical Research Letters*, *31*, L02611. https://doi.org/10.1029/2003GL018811

Tinti, E., Spudich, P., & Cocco, M. (2005). Earthquake fracture energy inferred from kinematic rupture models on extended faults. *Journal of Geophysical Research*, *110*, B12303. https://doi.org/10.1029/2005JB003644

Viesca, R. C., & Garagash, D. I. (2015). Ubiquitous weakening of faults due to thermal pressurization. *Nature Geoscience*, *8*(11), 875–879. https://doi.org/10.1038/ngeo2554

Wang, D., & Mori, J. (2016). Short-period energy of the 25 April 2015 M_w 7.8 Nepal earthquake determined from backprojection using four arrays in Europe, China, Japan, and Australia. *Bulletin of the Seismological Society of America*, *106*(1), 259–266. https://doi.org/10.1785/0120150236

Wang, Y., Day, S. M., & Denolle, M. (2017). Dynamic rupture models of the 2015 M_w7.8 Nepal earthquake, Abstract S31C-0831 Presented at 2017 Fall Meeting, AGU, San Francisco, CA, 11–15 Dec.

Wei, S., Chen, M., Wang, X., Graves, R., Lindsey, E., Wang, T., et al. (2018). The 2015 Gorkha (Nepal) earthquake sequence: I. Source modeling and deterministic 3D ground shaking. *Tectonophysics*, *722*, 447–461. https://doi.org/10.1016/j.tecto.2017.11.024

Weng, H., Huang, J., & Yang, H. (2015). Barrier-induced supershear ruptures on a slip-weakening fault. *Geophysical Research Letters*, *42*, 4824–4832. https://doi.org/10.1002/2015GL064281

Weng, H., & Yang, H. (2017). Seismogenic width controls aspect ratios of earthquake ruptures. *Geophysical Research Letters*, *44*, 2725–2732. https://doi.org/10.1002/2016GL072168

Weng, H., Yang, H., Zhang, Z., & Chen, X. (2016). Earthquake rupture extents and coseismic slips promoted by damaged fault zones. *Journal of Geophysical Research: Solid Earth*, *121*, 4446–4457. https://doi.org/10.1002/2015JB012713

Wibberley, C. A., & Shimamoto, T. (2005). Earthquake slip weakening and asperities explained by thermal pressurization. *Nature*, *436*(7051), 689–692. https://doi.org/10.1038/nature03901

Yagi, Y., & Okuwaki, R. (2015). Integrated seismic source model of the 2015 Gorkha, Nepal, earthquake. *Geophysical Research Letters*, *42*, 6229–6235. https://doi.org/10.1002/2015GL064995

Yang, H. (2015). Recent advances in imaging crustal fault zones: A review. *Earthquake Science*, *28*(2), 151–162. https://doi.org/10.1007/s11589-015-0114-3

Yang, H., Li, Z., Peng, Z., Ben-Zion, Y., & Vernon, F. (2014). Low velocity zones along the San Jacinto fault, Southern California, from body waves recorded in dense linear arrays. *Journal of Geophysical Research*, *119*, 8976–8990. https://doi.org/10.1002/2014JB011548

Yang, H., Liu, Y., & Lin, J. (2013). Geometrical effects of a subducted seamount on stopping megathrust ruptures. *Geophysical Research Letters*, *40*, 2011–2016. https://doi.org/10.1002/grl.50509

Yang, H., & Zhu, L. (2010). Shallow low-velocity zone of the San Jacinto fault from local earthquake waveform modeling. *Geophysical Journal International*, *183*(1), 421–432. https://doi.org/10.1111/j.1365-246X.2010.04744.x

Yang, H., Zhu, L., & Cochran, E. S. (2011). Seismic structures of the calico fault zone inferred from local earthquake travel time modelling. *Geophysical Journal International*, *186*(2), 760–770. https://doi.org/10.1111/j.1365-246X.2011.05055.x

Yin, J., Yao, H., Yang, H., Liu, J., Qin, W., & Zhang, H. (2017). Frequency-dependent rupture process, stress change, and seismogenic mechanism of the 25 April 2015 Nepal Gorkha Mw 7.8 earthquake. *Science China Earth Sciences*, *60*(4), 796–808.

Yu, H., Liu, Y., Yang, H., & Ning, J. (2018). Modeling earthquake sequences along the Manila subduction zone: Effects of three-dimensional fault geometry. *Tectonophysics*, *733*, 73–84. https://doi.org/10.1016/j.tecto.2018.01.025

Yue, H., Simons, M., Duputel, Z., Jiang, J., Fielding, E., Liang, C., et al. (2016). Depth varying rupture properties during the 2015 M_w 7.8 Gorkha (Nepal) earthquake. *Tectonophysics*, *714–715*, 44–54.